

# Temporal quantum interference in many-body programmable atom arrays

Madhumita Sarkar,<sup>1,\*</sup> Ben Zindorf,<sup>1,\*</sup> Bhaskar Mukherjee,<sup>2,1</sup> Sougato Bose,<sup>1</sup> and Roopayan Ghosh<sup>1,3,†</sup>

<sup>1</sup>*Department of Physics and Astronomy, University College London,  
Gower Street, WC1E 6BT, London, United Kingdom.*

<sup>2</sup>*Department of Physics, S.N. Bose Centre for Basic Sciences, Kolkata, 700106, India.*

<sup>3</sup>*School of Basic Sciences, Indian Institute of Technology, Bhubaneswar, 752050, India.*

Quantum superposition famously manifests as spatial interference, epitomized by the double-slit experiment. Its less explored temporal analogue, Stückelberg interference, arises in driven systems where phases accumulated along distinct time-domain pathways recombine. Extending this phenomenon to large interacting systems introduces a new complexity as delicate phase relationships are disrupted by many-body interactions. Here we experimentally achieve controllable vacuum-state freezing in programmable Rydberg arrays of up to 100 atoms through many-body Stückelberg interference, with visibility exceeding 70% and excitation suppression to 1% despite periodic driving that would typically induce heating. Comparing single and dual-frequency protocols across multiple geometries, we show that simultaneous modulation of detuning and Rabi frequency dramatically enhances interference-driven freezing. Finite-range interaction tails play a decisive role, producing interference patterns which constrained *PXP* models cannot capture. Our results establish temporal interference as a scalable microscopic mechanism for Floquet control, enabling predictive many-body state engineering in large-scale platforms.

## I. INTRODUCTION

Quantum interference lies at the heart of modern quantum science, underpinning technologies from lasers to quantum computation. The spatial version of interference, first demonstrated in Young’s double slit experiment and now in modern atom interferometers, provides the foundation for precision sensing and quantum control. Its temporal analogue offers an equally powerful yet far less explored resource. Rather than interfering across space, a non-monotonically driven system accumulates quantum phases along distinct time-domain pathways that subsequently recombine, creating interference without classical parallel. This time-domain interference extends the reach of spatial superposition, enabling continuous control of quantum evolution itself—offering new routes to suppress heating, accelerate state preparation, and stabilize driven phases inaccessible through static control. Its cleanest manifestation is in Landau–Zener–Stückelberg interference [1, 2] which serves as a fundamental testbed for the interference processes that govern Floquet engineering, where periodic driving suppresses or stabilizes excitations through constructive and destructive recombination across cycles. Whilst demonstrated in two-qubit systems in platforms such as superconducting qubits [3–6], trapped ions [7], quantum dots [8], ultracold atoms [9, 10] and single Rydberg atoms [11], its behaviour in large, strongly interacting ensembles and the microscopic mechanisms that govern it remain unexplored. Understanding how temporal interference survives many-body complexity is essential for predictive control in driven quantum systems.

Programmable Rydberg quantum simulators have emerged as a leading platform for exploring coherent quantum many-body dynamics [12], enabling discoveries such as quantum many-body scars [13], exotic quantum phases of matter [14] including topological spin liquids [15], quantum critical dynamics and Kibble-Zurek mechanisms [16], quantum optimization [17], and logical qubit encoding [18]. In parallel, Floquet engineering has emerged as a powerful approach for non-equilibrium control. Recent experiments have realized topological insulators in driven quantum processors [19], tailored Rydberg interactions through periodic modulation [20], and stabilized quantum many-body scars via non-equilibrium dynamics [21], while theoretical proposals have outlined pathways to exotic Floquet phases [22–28]. However, these achievements rest on empirically optimized protocols whose microscopic foundations remain obscure. The transformation of constructive and destructive interference among temporal pathways in the presence of long-range interactions, geometric constraints, and emergent correlations have not been systematically investigated. While theoretical works have proposed routes to dynamical freezing in idealized constrained many-body models [29, 30], no experiment has yet tested whether such approximations capture real interacting systems. The Rydberg platform, with its tunable interactions and programmable geometry, provides an ideal setting to uncover the microscopic foundations of temporal interference in many-body quantum matter.

Here, we demonstrate controllable vacuum-state freezing through many-body Stückelberg interference in programmable arrays of up to 100 Rydberg atoms, achieving interference visibility above 70% and excitation suppression down to 1% (dynamical freezing [31–33]), approaching the limits set by state-preparation and measurement (SPAM) errors. Across one-dimensional chains and two-dimensional lattices, we show how geometry shapes tem-

\* These authors contributed equally to this work

† roopayan@iitbbs.ac.in

poral interference, with dual-parameter driving (modulating both detuning and Rabi frequency) providing enhanced stabilization compared to single-parameter protocols. Crucially, finite-range interaction tails beyond the nominal blockade radius, typically neglected in constrained models, introduce geometry-dependent phase accumulation that reshapes interference patterns in ways *PXP*-type approximations cannot capture. Remarkably, vacuum stabilization persists even under low-frequency driving where standard Floquet theory predicts strong heating, demonstrating robustness beyond conventional expectations. We develop a Floquet perturbation framework that incorporates interaction-induced corrections, enabling predictive control of temporal interference in genuine many-body systems. Our results establish many-body Stückelberg interference as a scalable mechanism for non-equilibrium quantum control, laying the microscopic groundwork for Floquet engineering and programmable state preparation in strongly interacting platforms.

## II. PROGRAMMABLE RYDBERG PLATFORM AND DRIVE PROTOCOLS

We employ QuEra’s programmable neutral-atom quantum simulator, Aquila, which can host up to 256 Rydberg atoms with flexible geometry. For this work we restrict to systems of approximately 100 atoms. This scale is set jointly by device geometry and the finite probability of preparing defect-free arrays [34], which causes the likelihood of fully connected configurations to decrease with system size.

Each atom is encoded as a two-level system consisting of a stable electronic ground state  $|g\rangle$  and a high-energy Rydberg state  $|r\rangle$ . The collective vacuum state,  $|v\rangle$  corresponds to all atoms in  $|g\rangle$ . The system dynamics are governed by the Hamiltonian

$$H(t) = - \sum_i \Delta(t) n_i + \sum_i \frac{\Omega(t)}{2} \sigma_i^x + \sum_{i < j} \frac{C_6}{r_{ij}^6} n_i n_j, \quad (1)$$

where  $n_i = |r\rangle \langle r|_i$ ,  $\Delta(t)$  is the laser detuning,  $\Omega(t)$  the Rabi frequency, and the final term encodes van der Waals interactions between atoms separated by distance  $r_{ij}$ .

We probe temporal interference under two driving protocols. In the single-frequency case, the detuning is modulated sinusoidally,

$$\Delta(t) = \Delta_0 \cos(\omega t), \quad \Omega(t) = \Omega_0. \quad (2)$$

In the bi-frequency case, both detuning and Rabi coupling are modulated,

$$\Delta(t) = \Delta_0 \cos(\omega t), \quad \Omega(t) = \frac{\Omega_0}{2} [1 + \cos(r\omega t)], \quad (3)$$

with  $r = 0$  recovering the single-frequency protocol and  $r = 2$  introducing a second harmonic that enhances suppression of excitations and visibility of interference pattern. Higher harmonics can also be implemented, producing alternative interference patterns without altering

the underlying mechanism. The amplitudes  $\Delta_0$  and  $\Omega_0$  are chosen such that minima of the measured Rydberg density remain above the SPAM error bound, with visibility and fringe structure controlled systematically by tuning these values.

Together with programmable geometries, these protocols provide a controlled setting to explore how temporal interference emerges in large, strongly interacting Rydberg ensembles.

## III. ROBUST TEMPORAL INTERFERENCE IN ONE-DIMENSIONAL CHAINS

One-dimensional chains provide an ideal setting to uncover the microscopic physics of many-body temporal interference. We arrange 100 Rydberg atoms in a snake-like configuration with  $4.7 \mu\text{m}$  spacing (Fig. 1, top panels), initialize the system in the vacuum state  $|v\rangle$ , and measure the Rydberg excitation density  $n(T)$  after a single drive cycle. Using  $\Omega_0 = 2 \text{ rad}/\mu\text{s}$  and  $\Delta_0 = 20 \text{ rad}/\mu\text{s}$ , we observe pronounced oscillations in excitation density as the drive frequency  $\omega$  is varied. These frequency domain oscillations, analogous to spatial interference fringes in the double-slit experiment, arise from temporal interference between dynamical phases accumulated at successive passages through avoided level crossings during a drive cycle. At the first crossing, the system’s wavefunction coherently splits into components evolving along different energy branches, each accumulating a distinct dynamical phase as time progresses. When the system encounters the second crossing, these phases recombine and depending on their relative phase difference, interference can be constructive, i.e., yielding enhanced excitation, or destructive, i.e. leading to near complete suppression.

In our system, the enhanced Rydberg excitation corresponds to the “bright” fringes, while dynamical freezing of the vacuum represents the “dark” fringes. The resulting Stückelberg interference pattern extends coherently across the entire 100-atom array, demonstrating controllable vacuum stabilization in a strongly interacting many-body system.

The interference pattern reveals an unexpected detuning asymmetry that immediately signals departures from single-particle intuition. For positive detuning ( $\Delta_0 > 0$ ) (Fig. 1(a)), where  $|v\rangle$  represents an excited instantaneous eigenstate at  $t = 0$ , three distinct minima in  $n(T)$  emerge, matching predictions from the so called *PXP* (*PPXPP*) model—a minimal constrained model that enforces the Rydberg blockade by forbidding simultaneous excitation of nearest-neighbor (nearest- and next-nearest-neighbor) atoms [13]. In contrast, reversing the sign of detuning ( $\Delta_0 < 0$ ) (Fig. 1(b)), where  $|v\rangle$  is the instantaneous ground state, eliminates one of these minima, and shows strong finite-size effects for another in stark contrast to *PXP* results, yielding higher residual excitation even though the drive nominally begins from the lowest energy configuration. This inversion is striking: the system

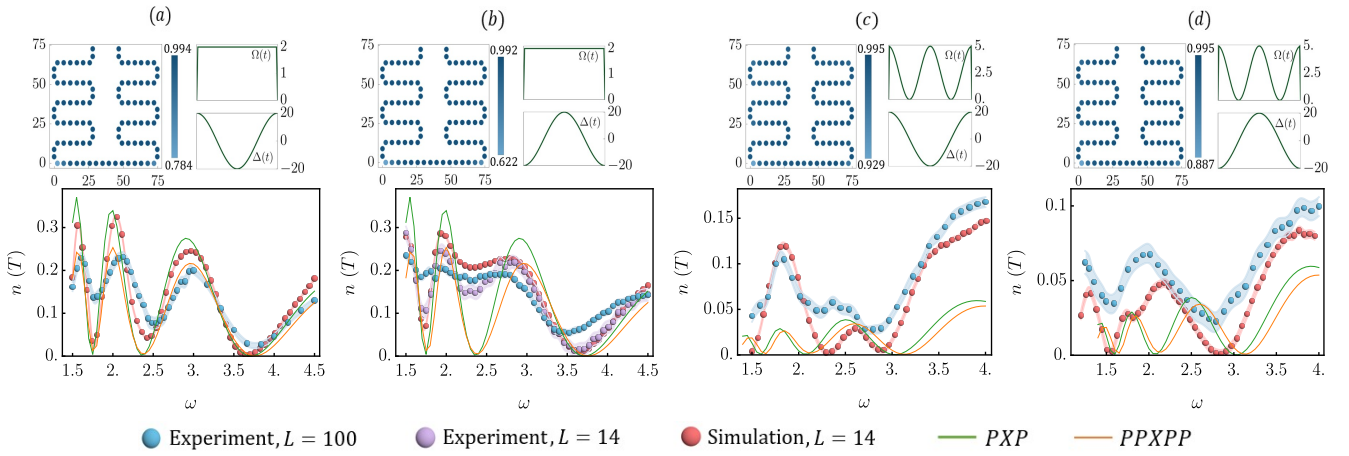


**FIG. 1. Many-body Stückelberg interference and vacuum freezing in one-dimensional chains.** Frequency-dependent Rydberg population  $n(T)$  in 100-atom chains ( $d = 4.7 \mu\text{m}$ ). **Top:** Snake geometry (positions in  $\mu\text{m}$  units) and drive protocols ( $\Omega$  in  $\text{rad}/\mu\text{s}$  units); shading shows atom loading probability. **a,b:** Single-frequency driving ( $\Omega$  constant). **c,d:** Bi-frequency driving ( $\Omega$  modulated). **a,c:**  $\Delta_0 > 0$  (vacuum as instantaneous excited state). **b,d:**  $\Delta_0 < 0$  (vacuum as instantaneous ground state). Blue circles: Experimental data obtained from Aquila quantum processor ( $L = 100$ ); purple: experimental data from a smaller system ( $L = 14$ , where shown); red: simulations from Bloqade (Classical simulator which simulates the full Rydberg Hamiltonian). Shaded regions indicate statistical uncertainty. Drive frequency  $\omega$  (in  $\text{rad}/\mu\text{s}$ ) controls interference fringes: minima correspond to destructive interference and vacuum freezing.

heats less when started from the excited eigenstate, and more when started from the ground state. The result violates the intuition that adiabatic initialization should preserve the vacuum better, revealing non-equilibrium interference unique to the driven many-body regime.

To quantify robustness of the fringes, we define their visibility  $V = (n^{\max} - n^{\min})/(n^{\max} + n^{\min})$  across a minima. In Fig. 1(a), at high frequencies ( $\omega \sim 3.5 \text{ rad}/\mu\text{s}$ ), the fringe achieves  $V \sim \frac{(0.2-0.026)}{0.2+0.026} \sim 0.77$ , indicating excellent destructive interference across all atoms. As frequency decreases, the contrast drops to  $V \sim 0.35$  at  $\omega \sim 1.5 \text{ rad}/\mu\text{s}$  for  $\Delta_0 > 0$ , and still lower for  $\Delta_0 < 0$ . This reduction partly arises from the finite  $4 \mu\text{s}$  coherence time of the device and partly due to strong finite size and geometry effects as can be seen in the comparison with  $L = 14$  experimental data. However, the persistence of clear dips even near this limit confirms the robustness of the Stückelberg process in a genuinely interacting ensemble.

We demonstrate how enhanced control is achieved through dual frequency driving in Fig. 1(c,d). Introducing a bi-frequency modulation,  $\Omega(t) = \frac{\Omega_0}{2}[1 + \cos(2\omega t)]$  with  $\Omega_0 = 5 \text{ rad}/\mu\text{s}$ , suppresses excitations across all frequencies. This effect is specially noticeable in the low frequency regime where despite the higher peak Rabi amplitude that would normally enhance fluctuations, Rydberg excitation density remains small. Additionally, the dip in  $n(T)$  is deeper in the high frequency regime showing further evidence that the second harmonic reinforces phase cancellations between successive passages through avoided crossings. This dual modulation extends beyond conventional Landau-Zener-Stückelberg interferometry, where only detuning is driven. By modulating both de-

tuning and coupling, we coherently control not just the energy gap but the transition matrix element itself, enabling enhanced interference stability.

However, constrained model simulations suffer from the same issues as for single frequency driving and overestimate the suppression magnitude, and particularly when  $|v\rangle$  is the ground state at  $t = 0$ , produces an additional spurious minima at  $\omega \sim 2.2$  lacking even in small size Blockade simulations. This suggests that higher-order interaction effects beyond the ideal blockade influence the phase accumulation significantly.

These discrepancies, can be explained analytically by computing the effective Floquet Hamiltonian for one full drive cycle (see Appendix E). At the lowest order in Floquet perturbation theory [35], both the constrained PXP model and the full Rydberg Hamiltonian exhibit effectively single-particle dynamics; each atom undergoes its own Stückelberg interference, with interactions merely forbidding adjacent excitations. This qualitatively explains why the basic interference structure is displayed. Within this approximation, the frequencies ( $\omega$ ) yielding dynamical freezing correspond approximately to zeros of the Bessel function  $J_0(\Delta_0/\omega)$  (see Appendix E). The distinction emerges beyond leading order. In the PXP model, we find that second-order Floquet corrections vanish entirely, leaving only single-particle like phase accumulation in this order and producing exceptionally stable destructive interference. The absence of second-order terms suppresses dephasing and heating channels, explaining the near ideal freezing observed in PXP dynamics. In real Rydberg systems, by contrast, finite-range van der Waals tails provide non-zero second-order contributions that generate genuine excitation creation pro-

cesses of the form  $V_{i,i+2} \sum_i \sigma_i^x n_{i+2} + \sigma_{i+2}^x n_i$ . These carry geometry and detuning dependent amplitudes, producing the observed pattern shifts and detuning asymmetries. Their presence demarcates the fortuitous single-particle like behavior of constrained models, which predict near perfect interference regardless of interaction details, from genuine many-body physics, where corrections depend sensitively on the full interaction landscape.

Introducing bi-frequency driving modifies this picture already at first order. The additional Rabi modulation changes how the system traverses the avoided crossing. Detuning and coupling now vary simultaneously, reshaping the instantaneous Hamiltonian throughout the passage. At first order in the Floquet expansion, an additional harmonic channel appears, with strength set by  $\mathcal{J}_r(\Delta_0/\omega)$ . When the Rabi frequency is modulated at twice the detuning frequency ( $r = 2$  in our protocol), the effective coupling during each avoided crossing is transiently reduced, suppressing the excitation amplitude accumulated in a single traversal.

This seemingly simple modification fundamentally alters the interference structure. Rather than a single oscillatory channel governing phase accumulation, bi-frequency driving activates multiple pathways, each contributing with distinct amplitudes determined by Bessel functions of the drive parameters, which is the mathematical signature of periodically driven quantum systems. The added second harmonic interferes destructively with the primary drive, suppressing residual excitations and deepening dynamical freezing. This additional cancellation pathway proves particularly valuable at low drive frequencies, where single-frequency protocols typically start showing heating effects. But by enabling interference across harmonics, the dual modulation sustains high-visibility fringes even for extended evolution times. However, not all modulation ratios produce such stabilization. The case  $r = 2$  is special. This can be explained via computing the first order perturbation terms where one can show that  $r = 2$  destructively interferes with the primary excitation channels whereas any general  $r$  does not do so (See Appendix E).

Finally, note that features governed by the lowest-order dynamics, resonance positions and bi-frequency enhancement, remain robust and universal. In contrast, fringe visibility and geometry-dependent modulation arise from higher-order processes that depend explicitly on the full interaction profile. This distinction between universal and tunable aspects establishes microscopic design principles for temporal control in interacting quantum matter, specially in Rydberg systems.

#### IV. INTERACTION-TUNED TEMPORAL INTERFERENCE

We next demonstrate how interatomic spacing controls St\"{u}ckelberg interference, revealing the crucial role of finite-range interactions in shaping temporal dynamics

(Fig. 2). Unlike constrained  $PXP$  models, where blockade radius changes negligibly affect interference minima, the full Rydberg Hamiltonian exhibits marked distance sensitivity due to van der Waals interaction tails that extend well beyond the nominal blockade radius.

At the interatomic spacings we probe ( $d = 4.7$  to  $5.3 \mu\text{m}$ ), next-nearest-neighbor interactions remain comparable to drive scales  $O(\Omega_0, \Delta_0)$ , i.e., we operate in a regime where interaction and drive energies compete directly, making interference patterns acutely sensitive to distance-dependent phase accumulation. The interference structure responds dramatically: at  $d = 4.7 \mu\text{m}$ , no destructive minimum appears near  $\omega \sim 2.4 \text{ rad}/\mu\text{s}$ , yet this feature emerges at  $d = 5.0 \mu\text{m}$ , with both Bloqade simulations and experiments confirming its onset despite its reduced visibility and slight shift of minima position. At a larger distance  $d = 5.3 \mu\text{m}$ , Bloqade predicts the strongest suppression of Rydberg excitations at  $\omega \sim 1.7 \text{ rad}/\mu\text{s}$ , a trend qualitatively reproduced in Aquila experiments for both  $L = 14$  and  $L = 100$ , though the visibility ( $V$ ) decreases with system size.

This distance sensitivity reveals how finite-range interaction tails continuously reshape temporal interference. As atoms separate, the relative contributions of nearest- and next-nearest-neighbor couplings shift, altering the accumulated phases that determine resonance conditions. Floquet perturbation theory (see Appendix E) quantifies this mechanism. Interaction-induced corrections to single-particle resonances depend explicitly on interatomic distance, producing the observed resonance migration that  $PXP$  models with fixed blockade radii miss entirely. Geometric tuning thus provides direct control over temporal interference patterns.

Complementing geometric control, we demonstrate tuning via detuning amplitude  $\Delta_0$  (Fig. 2, bottom). First-order Floquet perturbation theory predicts excitation suppression at zeros of the Bessel function  $J_0(\Delta_0/\omega)$ , yielding freezing frequencies that scale directly with  $\Delta_0$ . Experiments confirm this predicted scaling. The interference minima systematically shift to lower frequencies as  $\Delta_0$  decreases. However, as  $\Delta_0$  becomes sufficiently small, single-frequency driving loses effectiveness and visibility degrades—signaling entry into a non-perturbative regime where higher-order processes become important and richer dynamics emerge beyond the reach of lowest-order theory.

Together, these results establish that interatomic distance, geometry, and drive parameters form a multi-dimensional control space for engineering temporal interference. The ability to continuously tune freezing through both spatial arrangement and energetic parameters provides practical routes to stabilizing target quantum states and designing robust Floquet protocols in programmable platforms.

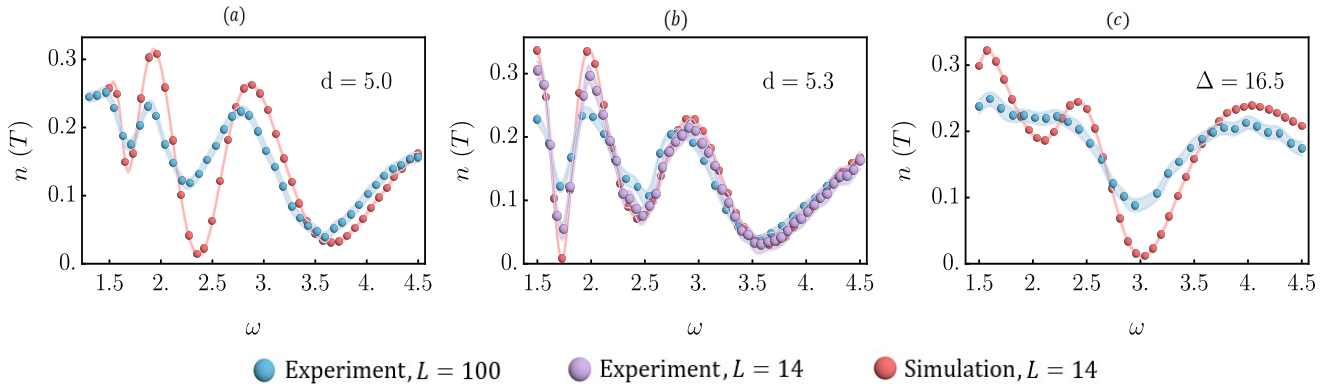


FIG. 2. **Tuning many-body interference by controlling interatomic distance and detuning.** Frequency-dependent Rydberg population  $n(T)$  in 100 atom chains reveals how interaction strength controls temporal interference. **a, b:** Varying interatomic spacing to  $d = 5.0$  and  $5.3 \mu\text{m}$  systematically shifts interference minima and modifies visibility, exposing the role of finite-range interaction tails in phase accumulation. **c:** Reducing detuning amplitude to  $\Delta_0 = 16.5 \text{ rad}/\mu\text{s}$  shifts minima to lower frequencies, consistent with Floquet perturbation theory. Blue circles: Experimental data obtained from Aquila quantum processor ( $L = 100$ ); purple: experimental data obtained from Aquila quantum processor on a smaller chain ( $L = 14$ , where shown); red: simulations from Bloqade (Classical simulator which simulates the full Rydberg Hamiltonian,  $L = 14$ ). Shaded regions indicate statistical uncertainty.

## V. TEMPORAL INTERFEROMETRY IN 2-D GEOMETRIES

Having established controllable temporal interference in one dimension through distance and detuning control, we turn to two-dimensional lattices, where each atom interacts with multiple neighbors acquiring geometry-dependent phases. These added interaction pathways pose a stringent test of whether coherent interference—and hence dynamical freezing—survives true many-body complexity. Additionally, in two dimensions, entanglement growth and long-range couplings render conventional tensor-network approaches inefficient, making experimental access particularly valuable. Figure 3 compares square and honeycomb geometries, with *Bloqade* simulations for  $L = 16$  atoms benchmarked against *Aquila* experiments at  $L = 100$  and standard *PXP* constrained model numerical simulations. As in the one-dimensional case, we initialize in the vacuum state with  $\Delta_0 = 20 \text{ rad}/\mu\text{s}$ .

Single-frequency driving exhibits striking reduction in visibility of fringes from one-dimensional systems. Square lattices retain vestiges of one visible interference fringe (possibly two for smaller system size as shown by the *Bloqade* result) though with highly reduced contrast compared to one-dimensional chains. Honeycomb lattices prove even more fragile. The patterns evident in small-scale simulations wash out at larger system sizes, particularly at low frequencies where finite coherence further suppresses visibility. This geometric hierarchy originates in next-nearest-neighbor (NNN) complexity. Honeycomb lattices possess six NNN couplings (at  $\sqrt{3}d$ ) compared to four in square lattices (at  $\sqrt{2}d$ ), creating a denser web of interaction-mediated phase pathways. Successful destructive interference then requires cancellation across

more competing channels, each contributing distance-dependent phases that must align precisely—a condition increasingly difficult to satisfy as connectivity and system size grow.

Dual-frequency modulation,  $\Omega(t) = \frac{\Omega_0}{2}[1 + \cos(2\omega t)]$  with  $\Omega_0 = 5 \text{ rad}/\mu\text{s}$  for Fig. 3, provides the rescue mechanism. In square lattices, excitation suppression recovers high-contrast interference with visibility  $V \sim \frac{0.055-0.004}{0.055+0.004} \sim 0.86$ , even exceeding one-dimensional performance. Additionally, in honeycomb lattices, where single-frequency driving fails, bi-frequency modulation stabilizes coherent patterns from  $L = 16$  to  $L = 100$ . The additional Rabi-frequency modulation introduces a secondary temporal interference channel that compensates for the intricate NNN phase network, and the patterns can be further improved by choosing smaller values of  $\Omega_0$ . Multi-frequency driving introduces additional interference channels with opposite-phase contributions that enhance destructive cancellation beyond single-frequency limits. This stabilization, however, relies on coherence between harmonics—only certain commensurate drive frequencies reinforce constructive cancellation, whereas incommensurate combinations introduce uncontrolled phase drifts

These results establish multi-frequency driving as essential for robust temporal interference in two-dimensional systems, where complex interaction networks demand multiple phase-matching conditions to maintain coherent cancellations.

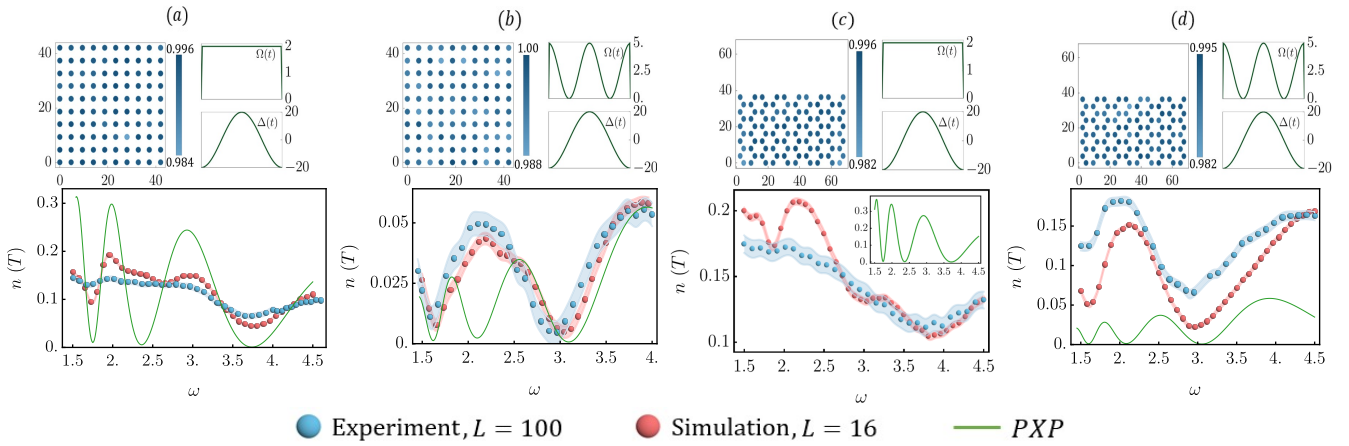


FIG. 3. **Temporal interference in two-dimensional geometries.** Frequency-dependent Rydberg population  $n(T)$  after one drive cycle in 2D arrays. **Top:** Atomic arrangements, drive protocols, and loading probabilities. **a,b:** Square lattice. **c,d:** Honeycomb lattice. **Panels (a,c):** Single-frequency driving produces weakened interference compared to 1D chains, with reduced visibility even in Bloqade simulations ( $L = 14$ , red) and further degradation in Aquila experiments ( $L = 100$ , blue). Green continuous curves denote PXP results. **Panels (b,d):** Dual-frequency modulation restores interference contrast, achieving visibility  $V > 0.9$  in square lattices and significant recovery in honeycomb. The superior square-lattice performance reflects simpler next-nearest-neighbor connectivity compared to the more complex honeycomb interaction network. Blue circles: Experimental data obtained from Aquila quantum processor ( $L = 100$ ); red: simulations from Bloqade (Classical simulator which simulates the full Rydberg Hamiltonian,  $L = 16$ ); green: numerical simulation of the constrained model (PXP).

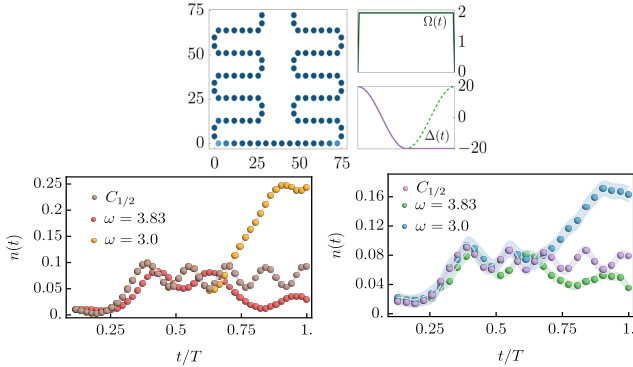


FIG. 4. **Microscopic dynamics within a drive cycle.** Time-resolved measurements reveal how Stückelberg interference produces vacuum-state freezing. **Top:** Experimental geometry and drive protocol. The purple line indicates the half-cycle control sequence, where the detuning is held fixed beyond  $t = T/2$ ,  $\Delta(t > T/2) = \Delta(T/2)$ . **Left:** Bloqade simulations ( $L = 14$ ) comparing constructive ( $\omega = 3.0$ , yellow) and destructive ( $\omega = 3.83$ , red) interference. Brown circles denote the half-cycle protocol ( $C_{1/2}$ ), which shows only residual oscillations and no interference signature. **Right:** Experimental verification on Aquila ( $L = 100$ ) at the same frequencies. The clear contrast between full-cycle (red/green and yellow/blue) and half-cycle (brown/purple) dynamics demonstrates that vacuum freezing arises from coherent amplitude recombination via second passage through the avoided crossing, rather than from an individual passage.

## VI. RESOLVING INTERFERENCE WITHIN INDIVIDUAL DRIVE CYCLES

The frequency-dependent vacuum freezing raises a fundamental question: how do quantum phases interfere across repeated passages to produce dynamical stability? To probe this microscopically, we track the time-resolved Rydberg population within a single drive cycle in 100-atom chains on Aquila (Fig. 4), benchmarked against Bloqade simulations at  $L = 14$ .

At frequencies yielding destructive interference ( $\omega \sim 3.825 \text{ rad}/\mu\text{s}$ ), the excitation probability rises approaching the first avoided crossing but falls during the second, completing the cycle with  $n(T) < 3\%$ —near-perfect vacuum recovery. In contrast, at constructive frequencies ( $\omega \sim 3.0 \text{ rad}/\mu\text{s}$ ), excitations accumulate coherently across both traversals, leading to final densities exceeding 15%.

To confirm that interference requires completion of the full temporal loop, we implement a truncated protocol halting evolution at half-period ( $t = T/2$ ), keeping  $\Delta$  fixed thereafter. In this case, the characteristic contrast vanishes. Excitation grows monotonically and settles into residual oscillations, demonstrating that the observed freezing originates from phase recombination across the full cycle, not from single-pass dynamics.

These time-resolved measurements directly visualize the Stückelberg mechanism at the many-body level. By resolving constructive and destructive recombination within each drive cycle of a 100-atom ensemble, our results establish temporal interference as a coherent, scalable mechanism underlying Floquet control in interacting

quantum systems.

## VII. OUTLOOK

Our demonstration of controllable many-body temporal interference opens several directions for quantum technologies. The sensitivity of interference patterns to sub-micron changes in interatomic spacing suggests applications in precision sensing, where collective Rydberg responses may provide enhanced metrological resolution. More broadly, the geometric tunability and bifrequency protocols we establish provides design principles for realizing heating-resistant Floquet engineering across quantum platforms.

Temporal interference also governs non-adiabatic quantum annealing, where systems traverse avoided crossings at finite speed. By engineering when dynamical phases accumulate versus cancel, one could accelerate quantum state preparation while maintaining high fidelity, offering advantages beyond conventional adiabatic schemes. This connection suggests that interference-based control of non-equilibrium dynamics represents a general resource for quantum optimization and algorithm design. Recent demonstrations of gate-engineered interference in digital quantum circuits [36] highlight the universality of these ideas across both analog and digital architectures, underscoring interference as a unifying paradigm for controlled quantum dynamics.

Finally, a central lesson from our work concerns the limits of simplified theoretical frameworks. Constrained models like PXP reproduce basic interference structures but systematically fail to capture the decisive role of finite-range interaction tails in controlling phase accumulation, heating, and visibility. We find quantitative agreement only in narrow parameter regimes where tails are effectively screened; elsewhere, the interplay of geometry, distance, and drive protocols reshapes interference in ways no truncated model predicts. This carries practical implications. Reliable Floquet control requires full

microscopic modeling rather than idealized constraints which presents a cautionary tale relevant across analog platforms: from Rydberg arrays to trapped ions and superconducting circuits. Whether appropriate design principles can be formulated into a universal framework for robust Floquet engineering for different platforms of quantum computing remains an open challenge. The microscopic foundation we provide represents a step towards that goal, transforming temporal interference from a greatly useful phenomenon into a predictive tool for quantum control in Rydberg systems.

## ACKNOWLEDGMENTS

This research used resources of the National Energy Research Scientific Computing Center (NERSC), a Department of Energy Office of Science User Facility under Contract No. DE-AC02-05CH11231 using NERSC award for QCAN Project DDR-ERCAP0033861. This project was also funded and supported by the UK National Quantum Computer Centre [NQCC200921], which is a UKRI Centre and part of the UK National Quantum Technologies Programme (NQTP). SB, MS and RG acknowledge EPSRC-SFI funded project EP/X039889/1 (GeQuantumBus). BZ was supported by the Engineering and Physical Sciences Research Council [grant numbers EP/R513143/1, EP/T517793/1]. B. M. was funded by Department of Science & Technology, Government of India via the INSPIRE Faculty programme. B.M was also funded by the European Research Council (ERC) under the European Union's Horizon 2020 research and innovation programme (Grant Agreement No. 853368), near the beginning of this project. The authors would like to thank Pedro Lopez, Milan Kornjača, Katherine Klymko and other members of the QuEra-NERSC team for discussions. RG and MS would like to thank Krishnendu Sengupta, Arnab Sen and Alexander Nico-Katz for discussions. BM would like to thank Krishnendu Sengupta and Dolev Bluvstein for discussions.

---

[1] S. Shevchenko, S. Ashhab, and F. Nori, Landau-zener-stückelberg interferometry, *Physics Reports* **492**, 1 (2010).

[2] O. V. Ivakhnenko, S. N. Shevchenko, and F. Nori, Nonadiabatic landau-zener-stückelberg-majorana transitions, dynamics, and interference, *Physics Reports* **995**, 1 (2023), nonadiabatic Landau-Zener-Stückelberg-Majorana transitions, dynamics, and interference.

[3] W. D. Oliver, Y. Yu, J. C. Lee, K. K. Berggren, L. S. Levitov, and T. P. Orlando, Mach-zehnder interferometry in a strongly driven superconducting qubit, *Science* **310**, 1653 (2005), <https://www.science.org/doi/pdf/10.1126/science.1119678>.

[4] D. M. Berns, W. D. Oliver, S. O. Valenzuela, A. V. Shytov, K. K. Berggren, L. S. Levitov, and T. P. Orlando, Coherent quasiclassical dynamics of a persistent current qubit, *Phys. Rev. Lett.* **97**, 150502 (2006).

[5] M. Kervinen, J. E. Ramírez-Muñoz, A. Välimäki, and M. A. Sillanpää, Landau-zener-stückelberg interference in a multimode electromechanical system in the quantum regime, *Phys. Rev. Lett.* **123**, 240401 (2019).

[6] P. Y. Wen, O. V. Ivakhnenko, M. A. Nakonechnyi, B. Suri, J.-J. Lin, W.-J. Lin, J. C. Chen, S. N. Shevchenko, F. Nori, and I.-C. Hoi, Landau-zener-stückelberg-majorana interferometry of a superconducting qubit in front of a mirror, *Phys. Rev. B* **102**, 075448 (2020).

[7] S. Gasparinetti, P. Solinas, and J. P. Pekola, Geometric landau-zener interferometry, *Phys. Rev. Lett.* **107**, 207002 (2011).

[8] F. Forster, G. Petersen, S. Manus, P. Hänggi, D. Schuh, W. Wegscheider, S. Kohler, and S. Ludwig, Characterization of qubit dephasing by landau-zener-stückelberg-majorana interferometry, *Phys. Rev. Lett.* **112**, 116803 (2014).

[9] U. Bengs, S. Patchkovskii, M. Ivanov, and N. Zhaborovkov, All-optical stückelberg spectroscopy of strongly driven rydberg states, *Phys. Rev. Res.* **4**, 023135 (2022).

[10] H. Wang, J. Chen, P. Fan, Y. del Castillo, A. Ferrón, L. Jiang, Z. Wu, S. Li, H.-J. Gao, H. Fan, J. Fernández-Rossier, and K. Yang, Electrically tunable quantum interference of atomic spins on surfaces, *Nature Communications* **16**, 8988 (2025).

[11] C. S. E. van Ditzhuijzen, A. Tauschinsky, and H. B. van Linden van den Heuvell, Observation of stückelberg oscillations in dipole-dipole interactions, *Phys. Rev. A* **80**, 063407 (2009).

[12] H. Bernien, S. Schwartz, A. Keesling, H. Levine, A. Omran, H. Pichler, S. Choi, A. S. Zibrov, M. Endres, M. Greiner, V. Vuletić, and M. D. Lukin, Probing many-body dynamics on a 51-atom quantum simulator, *Nature* **551**, 579–584 (2017).

[13] C. J. Turner, A. A. Michailidis, D. A. Abanin, M. Serbyn, and Z. Papić, Weak ergodicity breaking from quantum many-body scars, *Nature Physics* **14**, 745 (2018).

[14] S. Ebadi, T. T. Wang, H. Levine, A. Keesling, G. Semeghini, A. Omran, D. Bluvstein, R. Samajdar, H. Pichler, W. W. Ho, S. Choi, S. Sachdev, M. Greiner, V. Vuletić, and M. D. Lukin, Quantum phases of matter on a 256-atom programmable quantum simulator, *Nature* **595**, 227–232 (2021).

[15] G. Semeghini, H. Levine, A. Keesling, S. Ebadi, T. T. Wang, D. Bluvstein, R. Verresen, H. Pichler, M. Kalinowski, R. Samajdar, A. Omran, S. Sachdev, A. Vishwanath, M. Greiner, V. Vuletić, and M. D. Lukin, Probing topological spin liquids on a programmable quantum simulator, *Science* **374**, 1242–1247 (2021).

[16] A. Keesling, A. Omran, H. Levine, H. Bernien, H. Pichler, S. Choi, R. Samajdar, S. Schwartz, P. Silvi, S. Sachdev, P. Zoller, M. Endres, M. Greiner, V. Vuletić, and M. D. Lukin, Quantum kibble–zurek mechanism and critical dynamics on a programmable rydberg simulator, *Nature* **568**, 207–211 (2019).

[17] S. Ebadi, A. Keesling, M. Cain, T. T. Wang, H. Levine, D. Bluvstein, G. Semeghini, A. Omran, J.-G. Liu, R. Samajdar, X.-Z. Luo, B. Nash, X. Gao, B. Barak, E. Farhi, S. Sachdev, N. Gemelke, L. Zhou, S. Choi, and H. Pichler, Quantum optimization of maximum independent set using rydberg atom arrays, *Science* **376**, 1209–1215 (2022).

[18] D. Bluvstein, S. J. Evered, A. A. Geim, S. H. Li, H. Zhou, T. Manovitz, S. Ebadi, M. Cain, M. Kalinowski, D. Hangleiter, P. Bonilla, N. Maskara, I. Cong, X. Gao, P. S. Rodriguez, T. Karolyshyn, G. Semeghini, M. J. Gulans, M. Greiner, and V. Vuletić, Logical quantum processor based on reconfigurable atom arrays, *Nature* **626**, 58–65 (2023).

[19] M. Will, T. A. Cochran, E. Rosenberg, B. Jobst, N. M. Eassa, P. Roushan, M. Knap, A. Gammon-Smith, and F. Pollmann, Probing non-equilibrium topological order on a quantum processor, *Nature* **645**, 348 (2025).

[20] L. Zhao, M. D. K. Lee, M. M. Aliyu, and H. Loh, Floquet-tailored rydberg interactions, *Nature Communications* **14**, 7128 (2023).

[21] D. Bluvstein, A. Omran, H. Levine, A. Keesling, G. Semeghini, S. Ebadi, T. T. Wang, A. A. Michailidis, N. Maskara, W. W. Ho, S. Choi, M. Serbyn, M. Greiner, V. Vuletić, and M. D. Lukin, Controlling quantum many-body dynamics in driven rydberg atom arrays, *Science* **371**, 1355 (2021), <https://www.science.org/doi/pdf/10.1126/science.abg2530>.

[22] M. Bukov, L. D’Alessio, and A. Polkovnikov, Universal high-frequency behavior of periodically driven systems: from dynamical stabilization to floquet engineering, *Advances in Physics* **64**, 139 (2015), <https://doi.org/10.1080/00018732.2015.1055918>.

[23] T. Oka and S. Kitamura, Floquet engineering of quantum materials, *Annual Review of Condensed Matter Physics* **10**, 387 (2019).

[24] E. C. Domanti, D. Zappalà, A. Bermudez, and L. Amico, Floquet-rydberg quantum simulator for confinement in  $F_2$  gauge theories, *Phys. Rev. Res.* **6**, L022059 (2024).

[25] M. Sarkar, R. Ghosh, A. Sen, and K. Sengupta, Mobility edge and multifractality in a periodically driven aubry-andré model, *Phys. Rev. B* **103**, 184309 (2021).

[26] B. Mukherjee, S. Nandy, A. Sen, D. Sen, and K. Sengupta, Collapse and revival of quantum many-body scars via floquet engineering, *Phys. Rev. B* **101**, 245107 (2020).

[27] P. He, J.-X. Liu, H. Wu, and Z. D. Wang, Floquet amorphous topological orders in a one-dimensional rydberg glass, *Communications Physics* **8**, 237 (2025).

[28] S. Ghosh, I. Paul, K. Sengupta, and L. Vidmar, Destructive interference induced constraints in floquet systems, arXiv preprint arXiv:2508.18368 (2025).

[29] S. Kar, B. Mukherjee, and K. Sengupta, Tuning towards dynamic freezing using a two-rate protocol, *Phys. Rev. B* **94**, 075130 (2016).

[30] R. Ghosh, A. Sen, and K. Sengupta, Ramp and periodic dynamics across non-ising critical points, *Phys. Rev. B* **97**, 014309 (2018).

[31] A. Das, Exotic freezing of response in a quantum many-body system, *Phys. Rev. B* **82**, 172402 (2010).

[32] A. Haldar, D. Sen, R. Moessner, and A. Das, Dynamical freezing and scar points in strongly driven floquet matter: Resonance vs emergent conservation laws, *Phys. Rev. X* **11**, 021008 (2021).

[33] A. Haldar, A. Das, S. Chaudhuri, L. Staszewski, A. Wittek, F. Pollmann, R. Moessner, and A. Das, *Dynamical freezing in the thermodynamic limit: the strongly driven ensemble* (2024), arXiv:2410.11050 [cond-mat.stat-mech].

[34] J. Wurtz, A. Bylinskii, B. Braverman, J. Amato-Grill, S. H. Cantu, F. Huber, A. Lukin, F. Liu, P. Weinberg, J. Long, S.-T. Wang, N. Gemelke, and A. Keesling, *Aquila: Quera’s 256-qubit neutral-atom quantum computer* (2023), arXiv:2306.11727 [quant-ph].

[35] R. Ghosh, B. Mukherjee, and K. Sengupta, Floquet perturbation theory for periodically driven weakly interacting fermions, *Phys. Rev. B* **102**, 235114 (2020).

[36] Google Quantum AI and Collaborators, Observation of constructive interference at the edge of quantum ergodicity, *Nature* [10.1038/s41586-025-09526-6](https://doi.org/10.1038/s41586-025-09526-6) (2025).

## Appendix A: Experimental platform

Experiments were performed on QuEra’s programmable quantum processor, *Aquila* [34], which traps up to 256 individual  $^{87}\text{Rb}$  atoms in reconfigurable optical tweezer arrays. Each atom encodes a qubit between the ground state  $|g\rangle = |5S_{1/2}\rangle$  and a Rydberg state  $|r\rangle = |70S_{1/2}\rangle$ , coupled by a far-detuned two-photon transition (420 nm + 1013 nm). Pairs of Rydberg excitations interact via a van der Waals potential

$$V_{ij} = \frac{C_6}{r_{ij}^6}, \quad C_6 = 5,420,503 \text{ } \mu\text{m}^6 \text{ rad}/\mu\text{s},$$

(calibrated for  $|70S_{1/2}\rangle$ ). The maximum Rabi frequency which can be used is  $\Omega_0^{\max} = 15.6 \text{ rad}/\mu\text{s}$  (corresponding to  $\approx 2.48 \text{ MHz}$ ), which sets a characteristic static blockade radius for zero detuning, i.e.  $\Delta = 0$ ,

$$R_b = \left( \frac{C_6}{|\Omega_0^{\max}|} \right)^{1/6} \approx 8.4 \text{ } \mu\text{m}.$$

In our driven protocols  $\Omega(t)$  and  $\Delta(t)$  vary periodically, so the instantaneous blockade radius  $R_b(t) = (C_6/\sqrt{\Omega(t)^2 + \Delta(t)^2})^{1/6}$  is itself time-dependent over the cycle. Unless noted otherwise, quoted blockade values refer to  $t=0$ .

Atoms were optically pumped to the  $|g\rangle$  state with fidelity exceeding 99% before each experimental run. Finite site-loading imperfections introduce an average defect probability of  $p \approx 0.007$  per site. Thus it is expected that we obtain defect-free configurations in approximately 58% of attempts for  $\sim 100$ -atom arrays [34], subject to some corrections based on geometry. All reported data were obtained exclusively from verified defect-free realizations, identified via fluorescence imaging. To visualize geometry-dependent trapping reliability, the probability of successful atom loading is indicated by graded colour shading in the geometry figures shown in the main text. To ensure uniformity while maintaining experimental efficiency, we restrict all measurements to arrays containing 84–100 atoms across one- and two-dimensional geometries.

One-dimensional “snake” chains were limited by the  $75 \times 75 \text{ } \mu\text{m}^2$  active region of the device. At an interatomic spacing of  $d = 4.7 \text{ } \mu\text{m}$ , up to 100 atoms could be accommodated; increasing  $d$  to 5.0 and  $5.3 \text{ } \mu\text{m}$  reduced the usable system size to 88 and 84, respectively. Two-dimensional square and honeycomb arrays of comparable scale were realized under interatomic spacing of  $4.7 \mu\text{m}$  as well.

## Appendix B: Drive protocols

Time-dependent control of the detuning  $\Delta(t)$  and Rabi frequency  $\Omega(t)$  was implemented using piecewise-linear

waveforms with 50 ns temporal resolution. We employed two primary protocols:

$$\Delta(t) = \Delta_0 \cos(\omega t), \quad \Omega(t) = \frac{\Omega_0}{2} [1 + \cos(r \omega t)], \quad (\text{B1})$$

where  $r = 0$  (single-frequency) modulates only detuning with constant Rabi amplitude  $\Omega_0$ , and  $r = 2$  (dual-frequency) adds a commensurate Rabi modulation.

Drive angular frequencies spanned  $\omega = 1.2\text{--}4.5 \text{ rad}/\mu\text{s}$ , with most data taken between 1.5 and 4.5  $\text{rad}/\mu\text{s}$  so that single-cycle durations  $T = 2\pi/\omega \lesssim 4 \text{ } \mu\text{s}$  remain within the system coherence window reported in Aquila whitepaper [34]. Each cycle began and ended at  $\Omega = 0$ , with  $\sim 250 \text{ ns}$  rise and fall times set by hardware constraints.

A practical limitation at higher  $\omega$  is the fixed rise and fall overhead in  $\Omega(t)$ . Each cycle includes  $\sim 50 \text{ ns}$  ramps at both the beginning and end, amounting to a total overhead of  $0.1 \text{ } \mu\text{s}$  per period. The fractional time spent ramping,

$$f_{\text{ramp}} = \frac{2\tau_{\text{ramp}}}{T} = \frac{\tau_{\text{ramp}}\omega}{\pi},$$

increases linearly with drive frequency. Consequently, around 10% of each cycle is consumed by ramps at  $\omega = 4.5 \text{ rad}/\mu\text{s}$ , rendering still higher frequencies inefficient. Most experiments were therefore restricted to  $\omega \leq 4.5 \text{ rad}/\mu\text{s}$ , where the effective portion of the cycle used for coherent evolution exceeds 90%.

Typical control amplitudes were  $\Omega_0 = 2\text{--}5 \text{ rad}/\mu\text{s}$  and  $\Delta_0 = 20 \text{ rad}/\mu\text{s}$ , unless otherwise stated. All measurements report the Rydberg population after exactly one complete drive cycle ( $N = 1$ ).

## Appendix C: Measurement and error correction

Rydberg state populations were measured via fluorescence detection after each drive sequence, averaging over 300 defect-free shots per data point (corresponding to 700 – 1500 total attempts depending on loading probability). State-preparation and measurement (SPAM) errors were corrected using calibrated values  $\epsilon_{\text{det},g} = 0.01$  (false ground detection) and  $\epsilon_{\text{det},r} = 0.08$  (false Rydberg detection) [34]:

$$n(T) = \frac{n_{\text{meas}} - \epsilon_{\text{det},g}}{1 - \epsilon_{\text{det},g} - \epsilon_{\text{det},r}}. \quad (\text{C1})$$

Error bars in figures represent standard error of the mean computed from shot-to-shot fluctuations. Nearest-neighbour interatomic distances were uniform within each geometry to within  $\pm 50 \text{ nm}$ , except at snake-pattern bends where natural geometric variations occur.

## Appendix D: Numerical simulations

Numerical benchmarks for system sizes  $L = 14\text{--}16$  employed two complementary approaches. Full quantum

dynamics under the Rydberg Hamiltonian (Eq. (1)) were computed using BLOQADE, an open-source python package from QuEra for simulating neutral-atom quantum processors. Simulations retained the complete van der Waals interaction  $V_{ij} = C_6/r_{ij}^6$  between all atom pairs and employed identical time-discretized drive protocols as experiments.

For comparison with constrained models, we implemented PXP-type Hamiltonians that project out nearest-neighbor Rydberg excitations. Two variants were considered: PXP, which forbids only nearest-neighbor double occupancy, and extended-PXP (PPXPP), which additionally constrains next-nearest neighbors [30]. Time evolution employed second-order Trotterization with 400 steps per drive cycle, yielding relative errors below  $10^{-3}$ . Only parity symmetry was exploited to reduce computational cost; no other approximations were imposed.

System sizes up to  $L = 36$  were numerically accessible for certain geometries and parameter regimes; extended parameter scans are provided in Supplementary Information. All simulations employed open boundary conditions matching experimental geometries.

We note that in some parameter regimes, simulations predict excitation densities below 1%. This is a situation where experimental SPAM errors ( $\epsilon_{\text{det},g} \approx 0.01$ ) would dominate the signal. Parameters presented in the main text were therefore selected to balance optimal interference visibility with experimental observability, typically maintaining  $n(T) \gtrsim 0.02$  in destructive minima.

## Appendix E: Analytical understanding

To develop a microscopic understanding of the observed interference dynamics, we derive the effective Floquet Hamiltonian governing evolution over a single drive cycle. While alternative approaches—such as explicit Stückelberg phase accumulation or rotating-wave approximations—can describe isolated avoided crossings, the Floquet Hamiltonian method offers a simple and physically transparent route to characterize excitation dynamics over one complete driving period.

Exact calculation of the Floquet Hamiltonian,  $H_F$ , is intractable for large interacting systems such as Rydberg arrays (and even nontrivial for a single qubit under our protocol). We therefore adopt a *perturbative expansion formulated in the interaction picture*, a resummed variant of the standard Floquet–Magnus expansion that remains accurate even at intermediate drive frequencies, the *Floquet perturbation theory* [35]. We decompose the Hamiltonian as

$$H(t) = H_0(t) + H_1(t), \quad (\text{E1})$$

where  $H_1(t)$  acts as a perturbation to  $H_0(t)$ . Both terms may retain explicit time dependence; accuracy and convergence of the expansion depends on their relative energy scales as discussed in Ref. 35.

For our driven Rydberg system, we define

$$H_0(t) = \Delta(t) \sum_i n_i, \\ H_1(t) = \frac{\Omega(t)}{2} \sum_i \sigma_i^x + \sum_{|i-j| \geq 2} \frac{C_6}{r_{ij}^6} n_i n_j. \quad (\text{E2})$$

Nearest-neighbor interactions are excluded from  $H_1(t)$  because their magnitude far exceeds other energy scales and can be effectively integrated out by projecting the dynamics into the blockade subspace. The remaining next-nearest-neighbor and longer-range interactions, with strengths comparable to the drive amplitudes ( $O(\Omega_0, \Delta_0)$ ), constitute the leading corrections. As shown below, these finite-range terms are precisely what distinguish the full Rydberg dynamics from the constrained *PXP* model and govern the many-body deviations from ideal single-particle Stückelberg interference.

The Floquet perturbation expansion proceeds analogously to a Dyson series formulated in the interaction picture. The zeroth-order term defines the unperturbed evolution operator

$$U_0(T, 0) = e^{-iH_F^{(0)}T} = \mathcal{T} \exp \left[ -i \int_0^T H_0(t) dt \right], \quad (\text{E3})$$

where  $\mathcal{T}$  denotes time ordering. In our case  $H_0(t)$  is diagonal in the computational basis for all  $t$ , and therefore commutes with itself at different times. This eliminates the need for explicit time ordering, allowing direct integration,

$$U_0(t, 0) = \exp \left[ -i \int_0^T \Delta_0 \cos(\omega t) \sum_i n_i dt \right]. \quad (\text{E4})$$

$$= \exp \left[ -i \frac{\Delta_0}{\omega} \sin(\omega t) \sum_i n_i \right] \quad (\text{E5})$$

Clearly then  $U_0(T, 0) = I$ . To evaluate higher-order corrections, we transform the perturbation into the interaction picture,

$$H_1^I(t) = U_0^\dagger(t, 0) H_1(t) U_0(t, 0), \quad (\text{E6})$$

$$= \exp \left[ i\theta \sum_i n_i \right] H_1(t) \exp \left[ -i\theta \sum_i n_i \right] \quad (\text{E7})$$

where  $\theta = \frac{\Delta_0}{\omega} \sin \omega t$ . We can express the first- and second-order contributions to the Floquet operator as,

$$U_1(T, 0) = -i \int_0^T H_1^I(t) dt, = -iT \left[ \sum_i \Omega_0 \mathcal{J}_0\left(\frac{\Delta_0}{\omega}\right) \sigma_i^x + \sum_{\substack{i \\ k \geq 2}} V_k n_i n_{i+k} \right] \quad (\text{E8})$$

$$\begin{aligned} U_2(T, 0) &= (-i)^2 \int_0^T dt_1 H_1^I(t_1) \int_0^{t_1} dt_2 H_1^I(t_2) = (-i)^2 \frac{T^2}{2} \Omega_0^2 \mathcal{J}_0^2\left(\frac{\Delta_0}{\omega}\right) \sigma_i^x \sigma_j^x + (-i)^2 \Omega_0^2 \sum_{\substack{n=-\infty \\ n \neq 0}}^{\infty} \frac{T}{4n\omega} \mathcal{J}_{2n}^2\left(\frac{2\Delta_0}{\omega}\right) \sum_{i,j} \sigma_i^y \sigma_j^x \\ &+ (-i)^2 \Omega_0^2 \sum_{n=-\infty}^{\infty} \frac{T}{2(2n+1)\omega} \mathcal{J}_{2n+1}^2\left(\frac{\Delta_0}{\omega}\right) \sum_{i,j} \sigma_i^x \sigma_j^y + (-i)^2 \frac{T^2}{2} \Omega_0 \mathcal{J}_0\left(\frac{\Delta_0}{\omega}\right) \sum_i \sigma_i^x \sum_{\substack{j \\ k \geq 2}} V_k n_j n_{j+k} \\ &+ (-i)^2 \frac{T^2}{2} \Omega_0 \mathcal{J}_0\left(\frac{\Delta_0}{\omega}\right) \sum_{\substack{j \\ k \geq 2}} V_k n_j n_{j+k} \sum_i \sigma_i^x + (-i)^2 \frac{T}{n\omega} \Omega_0 \sum_n \mathcal{J}_n\left(\frac{\Delta_0}{\omega}\right) \sum_i \sigma_i^y \sum_{\substack{i \\ k \geq 2}} V_k n_i n_{i+k} \\ &- (-i)^2 \frac{T}{n\omega} \Omega_0 \sum_n \mathcal{J}_n\left(\frac{\Delta_0}{\omega}\right) \sum_{\substack{j \\ l \geq 2}} V_k n_j n_{j+l} \sum_i \sigma_i^y + (-i)^2 \frac{T^2}{2} \sum_{\substack{i \\ k \geq 2}} V_k n_i n_{i+k} \sum_j V_k n_j n_{j+k}, \end{aligned} \quad (\text{E9})$$

where  $\mathcal{J}_n(x)$  denotes the Bessel functions of first kind. This can be simplified using  $\mathcal{J}_{-n}(x) = (-1)^n \mathcal{J}_n(x)$  and  $\mathcal{J}_n(-x) = (-1)^n \mathcal{J}_n(x)$  as,

$$\begin{aligned} U_2(T, 0) &= -\Omega_0^2 \frac{T^2}{2} \mathcal{J}_0^2\left(\frac{\Delta_0}{\omega}\right) \sigma_i^x \sigma_j^x - 2 \frac{T^2}{2} \Omega_0 \mathcal{J}_0\left(\frac{\Delta_0}{\omega}\right) \sum_i \sigma_i^x \sum_j V_k n_j n_{j+k} - \frac{T^2}{2} \Omega_0 \mathcal{J}_0\left(\frac{\Delta_0}{\omega}\right) \sum_j V_k n_j n_{j+k} \sum_i \sigma_i^x \\ &- i \frac{T}{n\omega} \Omega_0 \sum_n \mathcal{J}_n\left(\frac{\Delta_0}{\omega}\right) \sum_{\substack{i \\ k \geq 2}} (V_k \sigma_i^x n_{i+k} + V_k \sigma_{i+k}^x n_i) - \frac{T^2}{2} \sum_{\substack{i \\ l \geq 2}} V_k n_i n_{i+l} \sum_j V_k n_j n_{j+k}. \end{aligned} \quad (\text{E10})$$

The corresponding effective Floquet Hamiltonian is then obtained via  $U(T, 0) = \exp[-iH_F T]$ , with  $H_F = H_F^{(0)} + H_F^{(1)} + H_F^{(2)} + \dots$ . We can now read off,

$$\begin{aligned} H_F^{(0)} &= 0, H_F^{(1)} = \left[ \sum_i \Omega_0 \mathcal{J}_0\left(\frac{\Delta_0}{\omega}\right) \sigma_i^x + \sum_{\substack{i \\ k \geq 2}} V_k n_i n_{i+k} \right] \\ H_F^{(2)} &= \frac{\Omega_0}{n\omega} \sum_n \mathcal{J}_n\left(\frac{\Delta_0}{\omega}\right) \sum_{\substack{i \\ k \geq 2}} (V_k \sigma_i^x n_{i+k} + V_k \sigma_{i+k}^x n_i) \end{aligned} \quad (\text{E11})$$

As shown above, we evaluate these terms explicitly for the single-frequency drive. When we have a bi-frequency drive protocol, the first order term modifies into,

$$\begin{aligned} U_1(T, 0) &= -iT \left[ \frac{\Omega_0}{2} \mathcal{J}_0\left(\frac{\Delta_0}{\omega}\right) \sum_i \sigma_i^x + \frac{\Omega_0}{2} \mathcal{J}_r\left(\frac{\Delta_0}{\omega}\right) \sum_i \sigma_i^x + \sum_{\substack{i \\ k \geq 2}} V_k n_i n_{i+k} \right], \end{aligned} \quad (\text{E12})$$

$r = 2$  in our case. Eq. E12 reveals how bi-frequency drive protocols, lead to multi-harmonic modulation which modifies excitation pathways already at first order.

However, the effective model discussed earlier fails to capture the non-monotonic dependence of the interference visibility on interatomic spacing, as it predicts only monotonic corrections in the second order with varying  $V$ . This indicates that a traditional Floquet perturbative expansion is insufficient and that higher-order processes must be re-summed in a more appropriate framework. To gain analytical insight, we perform a different resummation which we denote as *Fock-space Floquet Perturbation Theory* by reformulating the problem in Fock space. Here real space Rydberg excitation processes appear as a network of hopping processes between many-body configurations.

For clarity, we first consider a minimal three-site system, from which the generalization to larger arrays follows straightforwardly. In the blockade-projected subspace (open boundary conditions), the relevant basis states are  $|000\rangle, |001\rangle, |010\rangle, |100\rangle, |101\rangle$ . In this basis, the Hamiltonian takes the form

$$H = \frac{1}{2} \begin{pmatrix} 0 & \Omega_0 & \Omega_0 & \Omega_0 & 0 \\ \Omega_0 & 2\Delta_0 \cos(\omega t) & 0 & 0 & \Omega_0 \\ \Omega_0 & 0 & 2\Delta_0 \cos(\omega t) & 0 & 0 \\ \Omega_0 & 0 & 0 & 2\Delta_0 \cos(\omega t) & \Omega_0 \\ 0 & \Omega_0 & 0 & \Omega_0 & 2[V + 2\Delta_0 \cos(\omega t)] \end{pmatrix}, \quad (\text{E13})$$

where  $V \equiv V_{i,i+2}$  represents the next-nearest-neighbour (NNN) interaction.

We separate the Hamiltonian as

$$H_0 = \text{diag}(H), \quad H_1 = H - \text{diag}(H), \quad (\text{E14})$$

where  $H_1$  encodes the off-diagonal hopping terms between Fock states. The zeroth-order propagator,

$$U_0(t, 0) = \exp \left[ -i \int_0^t H_0(t'), dt' \right], \quad (\text{E15})$$

is diagonal in this basis, with each diagonal element corresponding to the accumulated phase of a specific Fock

configuration. Notably, one term, corresponding to the state  $|101\rangle$ , acquires an additional phase due to the finite interaction  $V$ ,

$$\langle 101 | U_0(t, 0) | 101 \rangle = \exp \left[ -2i \left( Vt + \frac{\Delta_0}{\omega} \sin(\omega t) \right) \right], \quad (\text{E16})$$

revealing that the NNN interaction explicitly modifies the dynamical phase landscape even at zeroth order. The inclusion of the finite interaction  $V$  profoundly alters the first-order dynamics by introducing new excitation channels absent in the strictly blockaded limit. This modification arises through the dynamical phase accumulated in the  $|101\rangle$  sector, which now explicitly enters the interaction-picture Hamiltonian,

$$H_1^I(t) = \frac{1}{2} \begin{pmatrix} 0 & \Omega_0 e^{-\frac{i\Delta_0 \sin(\omega t)}{\omega}} & \Omega_0 e^{-\frac{i\Delta_0 \sin(\omega t)}{\omega}} & \Omega_0 e^{-\frac{i\Delta_0 \sin(\omega t)}{\omega}} & 0 \\ \Omega_0 e^{\frac{i\Delta_0 \sin(\omega t)}{\omega}} & 0 & 0 & 0 & \Omega_0 e^{i(Vt - \frac{\Delta_0 \sin(\omega t)}{\omega})} \\ \Omega_0 e^{\frac{i\Delta_0 \sin(\omega t)}{\omega}} & 0 & 0 & 0 & 0 \\ \Omega_0 e^{\frac{i\Delta_0 \sin(\omega t)}{\omega}} & 0 & 0 & 0 & \Omega_0 e^{i(Vt - \frac{\Delta_0 \sin(\omega t)}{\omega})} \\ 0 & \Omega_0 e^{\frac{i\Delta_0 \sin(\omega t)}{\omega} - iVt} & 0 & \Omega_0 e^{\frac{i\Delta_0 \sin(\omega t)}{\omega} - iVt} & 0 \end{pmatrix}. \quad (\text{E17})$$

Evaluating the first-order propagator reveals two distinct excitation channels. The first corresponds to the familiar Stückelberg like process as seen in expansion above, proportional to  $-iT\Omega_0 \mathcal{J}_0(\Delta_0/\omega)$ , where  $\mathcal{J}_0$  denotes the zeroth-order Bessel function. The second, unique to systems with finite  $V$ , arises from the additional phase factor  $e^{-iVt}$ ,

$$\begin{aligned} & \int_0^T \Omega_0 e^{\frac{i\Delta_0 \sin(\omega t)}{\omega} - iVt} dt \\ &= 2\Omega_0 \sum_{n=-\infty}^{\infty} J_n \left( \frac{\Delta_0}{\omega} \right) e^{-i(V-n\omega)T/2} \frac{\sin[(V-n\omega)T/2]}{V-n\omega}. \end{aligned} \quad (\text{E18})$$

This expression exposes the physical origin of the distance-dependent interference modulation. The resonant enhancement occurs whenever  $V \approx n\omega$ , creating excitation channels that persist even at frequencies where  $\mathcal{J}_0(\Delta_0/\omega) = 0$ . These additional many-body channels

proliferate with system size, subtly reshaping the interference landscape but still remains sufficiently suppressed away from the resonances to preserve visibility of certain interference fringes even for 100-atom chains.

Evaluating these terms for the interatomic spacings used experimentally reproduces the observed trends. As the spacing increases from  $d = 5.0 \mu\text{m}$  to  $5.3 \mu\text{m}$ , the minimum near  $\omega \sim 1.7$  strengthens while that at  $\omega \sim 2.5$  weakens, consistent with the shift of  $V$  relative to  $\omega$ . Notably, in the  $V \rightarrow \infty$  limit these additional channels vanish—explaining why the ideal PXP model, which enforces perfect blockade, exhibits no such non-monotonic modulation. Thus, finite-range interactions act as a tunable perturbation that both enrich and complicate temporal interference, directly linking experimental distance control to the emergence of many-body Stückelberg structure.